5 GaSb–InAs Heterostructures

> When I hear of Schrödinger's cat, I reach for my gun.
>
> *(Steven William Hawking)*

5.1 Introduction

When in contact, GaSb and InAs have non-overlapping band gaps, which leads to a number of interesting phenomena in heterostructures created from these materials. Our group in Oxford has conducted extensive research on structures formed by alternating epitaxial GaSb and InAs layers grown by metal-organic vapour phase epitaxy (movpe). The purpose of Chapter 5 is to give an overview of these specimens both from a theoretical and a practical point of view.

These epitaxial strata are two-dimensional in the sense that they exhibit translational symmetry in the plane of the surface and the structure only changes along the perpendicular growth axis. In this thesis, the coordinate system is chosen such that the x and y axes lie parallel to the surface and the z axis points in the perpendicular direction. 'Parallel' refers to a direction in the (x, y)-plane, whereas 'perpendicular' or 'normal' refer to the z direction, as this direction is normal to the two-dimensional carrier systems which appear at the heterostructures and are the main focus of the present work.

The chapter starts out in Sec. 5.2 with a short reminder of subband energies in heterostructure quantum wells. In the following Sec. 5.3.1, a review of the 6·1 Å material system consisting of the nearly lattice-matched semiconductors InAs, GaSb, and AlSb and their het-

erostructures sets the stage for the discussion of the GaSb–InAs–GaSb double heterostructure (DHETS) studied in this thesis. After briefly touching the subject of InAs–AlSb quantum wells in Sec. 5.4, I shall concentrate on the peculiar broken-gap band line-up of GaSb–InAs heterostructures in Sec. 5.5 and explain how it leads to charge transfer, and—via quantization in the resulting electrostatic potential—to the formation of quasi-two-dimensional carrier gases. Electron–hole hybridization and the formation of the minigap are likewise discussed, hopefully clarifying the ramifications of this effect on observable properties, which will play a role in the remaining chapters.

Some remarks on Landau quantization and the in-plane charge transport in the presence of a perpendicular field follow in Sec. 5.6; while the focus is on sample characterization, they provide a useful reminder of some basic physical phenomena. Sec. 5.7 is dedicated to the growth of DHETS by MOVPE. A short introduction to the technology, which has not yet attained a high level of reproducibility, will allow the reader to better appreciate the limitations and uncertainties inherent in the creation of the samples discussed here. Finally, Sec. 5.8 will give an overview of the individual MOVPE-grown epitaxial structures discussed in this thesis for the purpose of reference. It will be pointed out how the observed properties of these samples can be understood in terms of the theoretical framework laid out earlier.

5.2 Subband Energies in a Heterostructure Quantum Well

The electrons and holes in a heterostructure quantum well experience a potential $V(z)$, where z is the position along the growth direction, but are free to move in the plane of the sample. Ignoring the influence of the crystal lattice, their wave functions are consequently of the form

$$\varphi(\mathbf{r}) = e^{i(k_x x + k_y y)} \chi(z), \tag{5.1}$$

where the envelope function $\chi(z)$ depends on z only. A form similar to Eq. (5.1) can still be found if the crystal lattice is taken into account, provided the interface potentials can be

neglected. This is know as the envelope function approximation [1]:

$$\varphi(\mathbf{r}) \approx \sum_{\alpha\in\{\text{GaSb,InAs}\}} e^{i(k_x x+k_y y)} u_{\alpha\mathbf{k}}(\mathbf{r})\chi(z), \tag{5.2}$$

where $u_{\alpha\mathbf{k}}$ is the Bloch function in material α.

As long as the effective masses in the materials forming the heterostructure are sufficiently similar, the Hamiltonian can be taken as

$$\hat{H} = \frac{\hat{\mathbf{p}}^2}{2\overline{m}^*} + V(z), \tag{5.3}$$

where $\hat{\mathbf{p}} = -i\hbar\nabla_{\mathbf{r}}$ is the momentum operator and $\overline{m}^*$ is the average effective mass. The resulting time-independent Schrödinger equation,

$$\hat{H}\varphi(\mathbf{r}) = E_{\text{tot}}\varphi(\mathbf{r}), \tag{5.4}$$

is separable if $\varphi(\mathbf{r})$ is given by Eq. (5.1) or (5.2), leading to a one-dimensional Schrödinger-like equation in $\chi(z)$:

$$\hat{H}_0\chi(z) = E_{\text{tot}}\chi(z), \tag{5.5}$$

where the one-dimensional Hamiltonian reads

$$\hat{H}_0 = -\frac{\hbar}{2\overline{m}^*}\frac{\partial^2}{\partial z^2} + V(z) + E_{xy} \tag{5.6}$$

and E_{xy} is the in-plane kinetic energy resulting from the corresponding equation in x and y—in the free electron case, this would be $\hbar(k_x^2 + k_y^2)/2\overline{m}^*$. Eq. (5.5) leads to localized envelope functions $\chi_n(z)$ with corresponding subband energies $E_n = E_{\text{tot}} - E_{xy}$, depending on the shape of the potential $V(z)$.

5.3 The 6·1 Å Family of III–V Semiconductors: InAs, GaSb, AlSb

5.3.1 Bulk Material Properties

InAs, GaSb, and AlSb crystallize in the familiar zincblende structure shown in Fig. 5.1, which consists of two interleaved face-centred cubic sublattices [2]. The lattice constant for all three

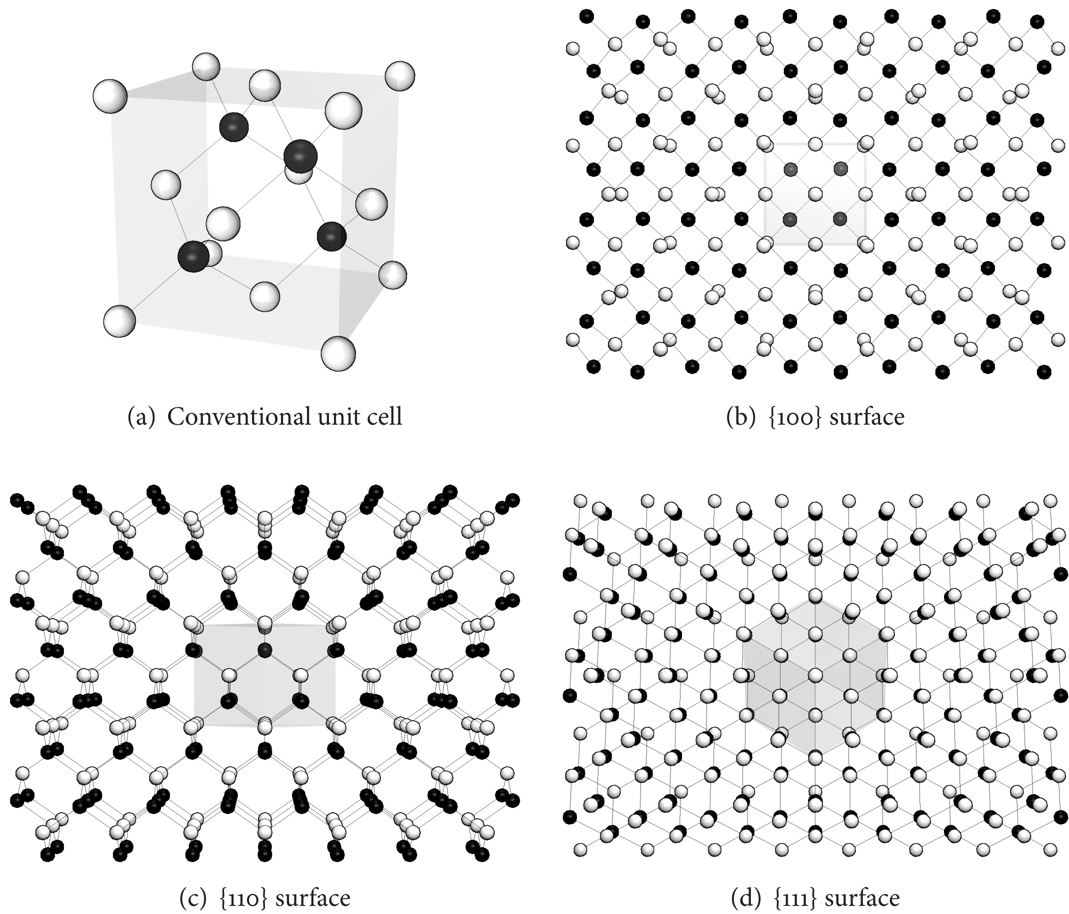

Figure 5.1: The zincblende structure. Black and white spheres represent atoms of different species. Both sublattices are equivalent. Bonds are shown as thin black lines.

materials is around 6·1 Å, so that lattice-matched heterostructures can be grown [3]; the exact lattice spacings are 6·0584 Å for InAs, 6·0959 Å for GaSb, and 6·1355 Å for AlSb at 300 K [4]. Like GaAs, the materials preferentially cleave along the {110} family of planes.

The reciprocal lattice of the face-centred cubic lattice, and hence the diamond and zincblende lattices, is a body-centred cubic lattice. The Wigner-Seitz unit cell of the reciprocal lattice, which corresponds to the first Brillouin zone, forms a truncated octahedron and is shown in Fig. 5.2(a) with its conventionally labelled symmetry points [2, 4, 5].

There are eight outer electrons per primitive unit cell—3 from the group III element (In, Ga, or Al) and 5 from the group V element (As or Sb)—which occupy four bonding sp^3

hybrid orbitals. The main features of the full band structure are shown in Fig. 5.2. Bulk InAs and GaSb are direct-gap semiconductors, since both the maximum of the valence band and the minimum of the conduction band lie at the Γ-point. The size of the energy gap is $E_g^{(InAs)} \approx 415\,\mathrm{m}e\mathrm{V} - 0{\cdot}276\,\mathrm{m}e\mathrm{V\,K^{-1}} \times T^2/(T - 83\,\mathrm{K})$ for InAs [9] and $E_g^{(GaSb)} \approx 813\,\mathrm{m}e\mathrm{V} - 0{\cdot}108\,\mathrm{m}e\mathrm{V\,K^{-1}} \times T^2/(T - 10{\cdot}3\,\mathrm{K})$ for GaSb [10]. Bulk AlSb is an indirect-gap semiconductor with the bottom of the conduction band at the X-point and $E_g^{(AlSb)} \approx 1696\,\mathrm{m}e\mathrm{V} - 0{\cdot}390\,\mathrm{m}e\mathrm{V\,K^{-1}} \times T^2/(T + 140\,\mathrm{K})$ [11]. At 300 K, the energy gaps are 350 meV for InAs, 727 meV for GaSb, and 1616 meV for AlSb, while at 4·2 K the values are close to their zero-temperature limits of 813 meV, 415 meV, and 1696 meV, respectively.

As there are eight electrons in bonding states, four spin-degenerate valence bands are filled: a single band corresponding to the atomic *s* orbital and three bands corresponding to the three *p* orbitals. The latter take part in conduction and are split by spin–orbit interaction into a 'split-off' hole band with total angular momentum $J = \frac{1}{2}$ and two 'heavy' and 'light' hole bands with $J = \frac{3}{2}$, which are degenerate at the Γ-point. The lowest conduction band corresponds to the next highest *s* orbital and is therefore singly degenerate (disregarding spin degeneracy).

5.3.2 Heterostructure Band Alignment

The band line-ups in heterostructures combining these materials, shown schematically in Fig. 5.3, differ drastically from those available in the widely studied GaAs–$Al_xGa_{1-x}As$ system. While the GaSb–AlSb heterojunction is characterized by a conventional type I band alignment in which the narrow gap material has both a higher valence and lower conduction band than the wide gap material, the AlSb–InAs and GaSb–InAs systems exhibit a staggered, or type II alignment [3]. The InAs–AlSb conduction band offset at *c.* 1·35 eV is exceptionally large compared to other practical semiconductor heterojunctions, facilitating very deep quantum wells and very high tunnelling barriers. The most remarkable band alignment,

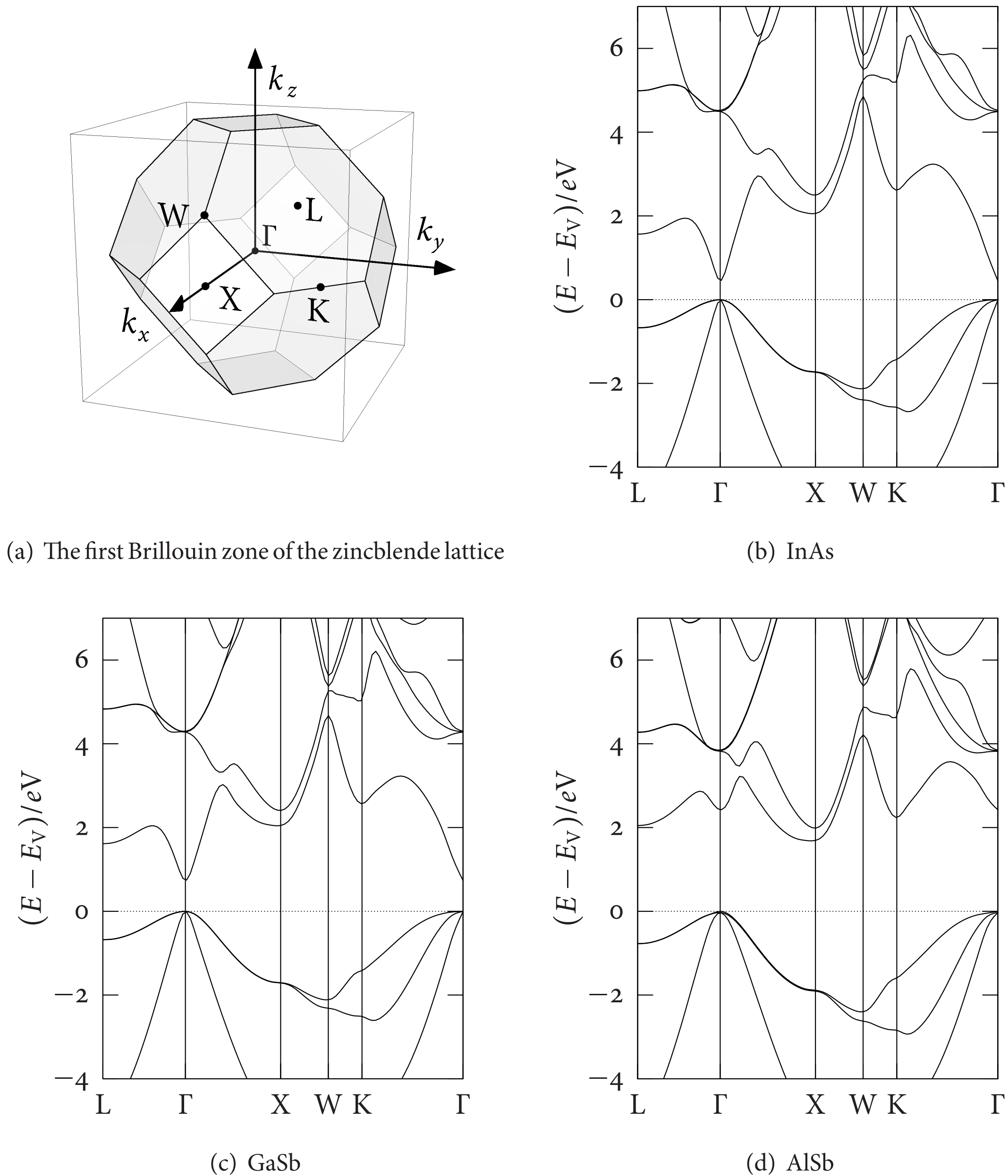

(a) The first Brillouin zone of the zincblende lattice

(b) InAs

(c) GaSb

(d) AlSb

Figure 5.2: bulk InAs, GaSb, and AlSb. The calculation uses the empirical pseudopotential method following Cohen *et al.* [6]. The parameters for AlSb are taken from Topol *et al.* [7]. Spin-orbit interactions and non-local correction terms are not considered; more realistic calculations are available in the literature [8].

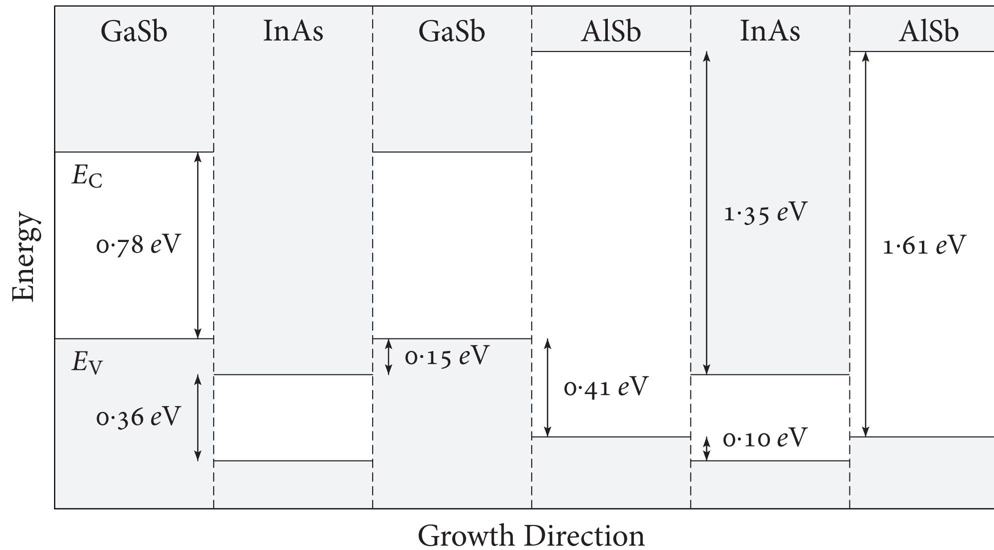

Figure 5.3: InAs, GaSb, and AlSb at room temperature. Adapted from KROEMER [3].

however, is that of GaSb–InAs heterointerfaces: The bottom of the InAs conduction band lies approximately 150 m*e*V below the top of the GaSb valence band, leading to a *broken gap* line-up [12], a configuration that is sometimes classified as 'type III'.

5.3.3 Sample Growth

Starting from initial work at IBM [12], the growth of the 6·1 Å materials by molecular beam epitaxy (MBE) has been developed systematically by a number of researchers, including HERBERT KROEMER's group at the UNIVERSITY OF CALIFORNIA [13–15], and can now be regarded as a fairly mature process.

Another viable option is MOVPE, and our research group at Oxford has demonstrated the growth of high quality GaSb–InAs heterostructures [16, 17] using the methods documented in Sec. 5.7. In particular, GaSb–InAs heterostructures which are nearly intrinsic, *i.e.*, in which carriers are created mostly by charge transfer between the GaSb and InAs layers as explained in Sec. 5.5.1, are grown more readily using this technique [18, 19]. However, the deposition of AlSb by MOVPE remains problematic, as most of the potential metal-organic precursors result in high levels of carbon and oxygen contamination. With alternative sources it has been dif-

ficult to control gas phase reactions, making them unsuitable for atmospheric pressure reactors and restricting the combinations of precursors that can be used simultaneously [20–22].

5.3.4 Interface Configuration

At a heterojunction between two semiconductors that do not share a common species, two distinct bond configurations are possible. For example, an atomically flat GaSb-InAs interface may consist of either In–Sb bonds or Ga–As bonds. Which kind of bond is formed depends on the details of the growth process. Methods have been developed for both MBE [14] and MOVPE [23] to control the interface composition to a certain degree. However, even for MBE-grown samples the interface flatness and the preference for one bond will not be perfect.

The two interfaces are not equivalent: Interface states differ, and the different equilibrium bond lengths cause different strain distributions. There is also theoretical and experimental evidence that the band offset at the GaSb–InAs heterojunction depends on the bond configuration [24, 25]. The situation is further complicated by the influence of the bonding type–or the methods used to impose it–on the growth processes. The abruptness of the interface and the chemical composition of nearby layers may be affected, and the effect can depend on the ordering of the materials, with significantly different behaviour at the upper and lower interfaces of a quantum well [14, 26].

5.4 InAs–AlSb Heterostructures

The large conduction band offset between InAs and AlSb in combination with the high electron mobility in InAs suggests that it is possible to grow very deep quantum wells containing high-density, high-mobility two-dimensional electron gases (2DEGs) with potential applications to high-speed field-effect transistors (FETs). Considerable effort has been devoted to the optimization of such structures, and mobilities as high as 220,000 $\mathrm{cm^2/(V\,s)}$ at sheet densities of $5{\cdot}5 \times 10^{12}\,\mathrm{cm^{-2}}$ have been obtained [3].

For narrow InAs wells, the mobility is limited by interface roughness scattering and depends sensitively on the interface composition [13, 27]. Experimentally, it was found that predominantly InSb-like interfaces yield higher mobilities and that the heterojunction below the quantum well has a greater influence [13, 14, 26, 28].

Nominally undoped InAs–AlSb quantum wells can have high electron sheet concentrations of the order 10^{12} cm^{-2}, much in excess of what can be explained by background doping. Because of the depth of the quantum well, which reaches almost down to the AlSb valence band, electrons drain readily into the InAs layer. It has been shown by Nguyen *et al.* [15] that a large fraction of the carrier concentration results from donor states at the surface of the GaSb cap that protects the top AlSb barrier from oxidation. Other proposed sources of excess electrons include Al_{Sb} antisite defects [13] and interface Tamm states [3]. Intentional modulation doping is achieved by embedding a heavily doped layer of AlSb:Te [29] or thin InAs:Si [30] in one or both of the barriers.

Heterostructure fets (hfets) with cut-off frequencies of up to 93 GHz have been demonstrated by Bolognesi *et al.* [30–32]. The long mean free paths of the order 10 μm also make high-mobility InAs–AlSb quantum wells attractive model systems for studying ballistic transport in quantum constrictions at low temperatures [33, 34].

5.5 Broken-Gap Heterostructures

5.5.1 Effective Band Gap and Charge Transfer

The broken-gap band line-up of InAs and GaSb makes it possible to create both semiconducting and semimetallic heterostructures with tunable virtual band gaps. As long as the confinement energy of the carriers in the effective electrostatic potential of the heterostructure is small, electrons can lower their energy by dropping from the GaSb valence band to the InAs conduction band until the Fermi level E_F is equal in both layers and the system is in equilibrium. This charge transfer is illustrated in Fig. 5.4 for a symmetric GaSb–InAs–

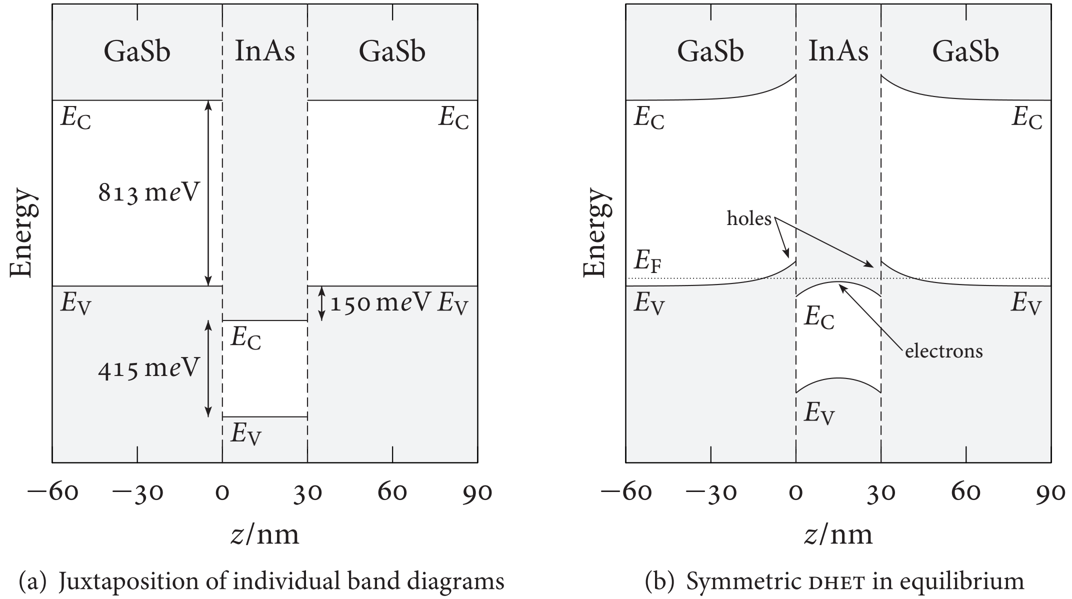

(a) Juxtaposition of individual band diagrams

(b) Symmetric DHET in equilibrium

Figure 5.4: Band alignment of a GaSb–InAs–GaSb DHET with a 30 nm InAs layer

GaSb DHET similar to the samples studied in this thesis. If the GaSb layer is replaced by a GaSb–AlSb superlattice [35] or an AlSb spacer layer is introduced between the GaSb and InAs layers [36], the charge transfer process can still take place, leaving behind mobile holes in the superlattice or the GaSb layer, respectively.

For narrow well widths, the lowest electron subband energy lies above the highest hole level and the heterostructure is a semiconductor. For wells wider than roughly 85 Å [16, 37], however, charge transfer is energetically favourable and the structures exhibit semimetallic behaviour. The GaSb–InAs–GaSb DHETs studied in this thesis have InAs layers 240 to 300 Å wide and fall well within the latter regime. It is also possible to tune the effective band gap by replacing the GaSb with $Al_xGa_{1-x}Sb$ and varying x.

The initial work on broken-gap heterostructures focused on the semimetal–semiconductor transition and the band gap engineering possibilities in superlattice structures [12, 38]. However, the practical usefulness of the tunable band gap is restricted by the fact that the electrons and holes are spatially separated and only the proportion of the device volume in which their wave functions overlap is optically active [3]. As the effective band gap can be

made arbitrarily small, and in particular smaller than the binding energy E_X of an exciton, it was also suggested that broken-gap heterostructures with an excitionic ground state can be created and used to study exciton gases [39]. However, evidence for an excitonic ground state remains elusive. Cyclotron resonance features originally attributed to excitons [40] are better explained by electron–hole hybridization (*cf.* Sec. 5.5.3), as demonstrated in experiments using AlSb barrier layers between the GaSb and InAs layers to control the wave function overlap and hence the hybridization gap [36].

Because of the quantization of the envelope wave function in the growth direction, the carrier sheets in semimetallic heterostructures form quasi-two-dimensional electron gases (2DEGs) and quasi-two-dimensional hole gases (2DHGs) [38, 41, 42]. These strongly interacting 2D carrier gases have attracted much interest and are also the essential feature of broken-gap systems from the point of view of the present work.

5.5.2 Band Bending and Electron-Hole Ratio

In an intrinsic heterostructure, all carriers are created by charge transfer from the GaSb to the InAs layers and the sheet densities of mobile electrons and holes are the same. In actual samples, localized states at interfaces, defects, or the sample surface can act as donors or acceptors, potentially resulting in unbalanced concentrations of mobile carriers.

For a large number of experiments it is useful to be able to control the electron–hole ratio. While a limited control of the carrier concentrations is possible by optical pair generation [13, 27] or application of hydrostatic pressure [43, 44], the most flexible and conceptually most simple approach is the use of a gate electrode [45]. The energy bands bend to an extent determined by the voltage at the gate and the screening within the structure. As a result, the position of the Fermi level at the depth of the carrier gases can be changed over a considerable range. However, gating of heterostructures with GaSb top layers represents a certain technological challenge as high quality insulating layers cannot be grown by thermal oxidation of GaSb and even Schottky contacts are difficult to form reliably on this material.

Successful fabrication of insulated gates has been reported using anodic oxide [17, 46] as well as deposited polymers [35, 47] or oxides [48, 49]. Depleting the lower carrier sheet may also necessitate the use of a back gate to avoid the screening caused by the upper sheet [47]. Using top gates, Drndic *et al.* [35] have demonstrated the change from electron-dominated to hole-dominated conduction in a single structure. Yang *et al.* [48] have explored the non-monotonic transfer characteristic associated with this transition in a FET-like device.

Magnetotransport studies of GaSb–InAs–GaSb DHETs grow by MOVPE in Oxford [25, 50, 51] indicate that the electron density is always higher than the hole density. These DHETs lie relatively close (40 to 120 nm) to the surface of the semiconductor, and there is compelling evidence that the increased electron–hole-ratio is caused by surface states at the GaSb–air interface, which pin the Fermi level at a position different from its bulk value.

While the precise position of the surface pinning is generally not known and depends on the chemical composition of the interface, there is some evidence [52] that for surfaces covered with native oxide the Fermi level lies in the lower part of the band gap but above the Fermi level in the bulk material. As a result of the Fermi level pinning, the bands bend towards lower energy near the surface, and if the GaSb cap layer is sufficiently thin, the DHET lies in a region of strong band bending as illustrated in Fig. 5.5(a). The pulling down of the band configuration with respect to the Fermi level E_F means that more conduction band states in the InAs lie below E_F and fewer valence band states in the GaSb lie above E_F, leading to the observed electron–hole imbalance as illustrated in Fig. 5.5(b). The mechanism is hence expected to lead to a dependence of the electron–hole ratio on the GaSb cap thickness, which has been observed experimentally [51]. This dependence affords a limited control over the electron–hole ratio without the use of an insulated gate and should in principle make it possible to impose a potential and carrier density modulation on the carrier sheets by laterally varying the cap layer thickness.

The band bending induced by the surface states means that the DHET is no longer symmetrical. In fact, the GaSb valence band edge at the upper interface lies close to the Fermi energy, and it is questionable whether there are any mobile holes in the cap layer at all [51]. Another

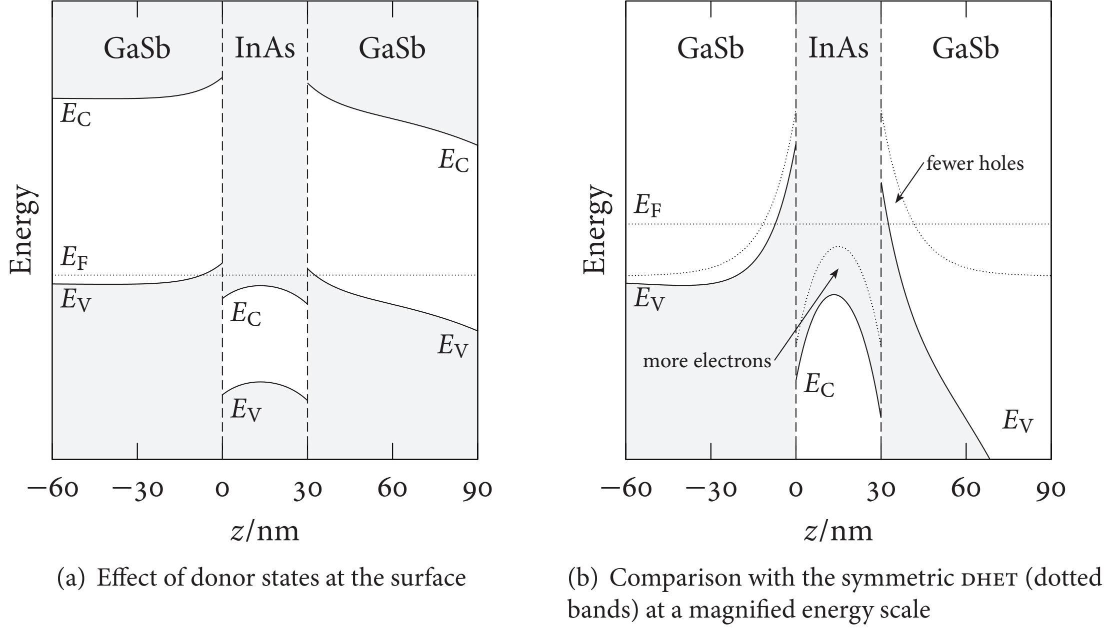

(a) Effect of donor states at the surface

(b) Comparison with the symmetric DHET (dotted bands) at a magnified energy scale

Figure 5.5: Band bending due to surface states

possible source of band asymmetry is the dependence of the band overlap on the GaSb–InAs interface composition: As both the group III and the group V elements change at the interface, either a monolayer of InSb or GaAs may be formed, and it has been shown that interfaces that are predominantly of the GaSb type have a band overlap approximately 30 meV smaller than those of the InSb type [44, 53]. If the interface types on both sides of the InAs layer are different, the resulting DHET will have an asymmetric band line-up even in the absence of surface states [25]. The samples discussed in this thesis did not have interfaces biased either towards InSb or GaSb, but the presence of a residual imbalance could not be excluded.

5.5.3 Hybridization and Minigap

The electron and hole dispersion relations $E_i(\mathbf{k})$, where $\mathbf{k}$ is the in-plane wave vector and i identifies the band, overlap as a result of the band alignment described in Sec. 5.3.2. Any finite coupling $\Delta_{ij}/2$ between electron and hole states will therefore lead to the formation of an energy gap Δ_{ij} at the crossing points. A simple two-band model can be used to capture

the essential behaviour of the hybridized system [42, 54]: In this model, the electron band is assumed to be isotropic and is given by

$$E_{\mathrm{e}}(\mathbf{k}) = \frac{\hbar^2 \mathbf{k}^2}{2m^*}, \tag{5.7}$$

where $m^* = 0{\cdot}03 m_{\mathrm{e}}$ is the electron effective mass, while the warped heavy hole band is

$$E_{\mathrm{h}}(\mathbf{k}) = E_{\mathrm{g}} - \frac{\hbar^2}{m_{\mathrm{e}}} \left(|A| \mathbf{k}^2 - \sqrt{B^2 \mathbf{k}^4 + C^2 k_x^2 k_y^2} \right), \tag{5.8}$$

where E_{g} is the band overlap and $A = -14{\cdot}3$, $B = -10{\cdot}4$, and $C = 13{\cdot}5$ are anisotropy parameters [55]. The Schrödinger equation for the coupled system leads to the eigenvalue problem

$$\begin{pmatrix} E_{\mathrm{e}}(\mathbf{k}) & \Delta_{\mathrm{eh}}/2 \\ \Delta_{\mathrm{eh}}/2 & E_{\mathrm{h}}(\mathbf{k}) \end{pmatrix} \begin{pmatrix} c_{\mathrm{e}} \\ c_{\mathrm{h}} \end{pmatrix} = E(\mathbf{k}) \begin{pmatrix} c_{\mathrm{e}} \\ c_{\mathrm{h}} \end{pmatrix}, \tag{5.9}$$

where c_{e} and c_{h} are the coefficients of the electron and hole wave functions, respectively. The mixed energy bands obtained by solving Eq. (5.9) are

$$E_{\pm}(\mathbf{k}) = \frac{1}{2} \left[E_{\mathrm{e}}(\mathbf{k}) + E_{\mathrm{h}}(\mathbf{k}) \right] \pm \frac{1}{2} \sqrt{\left[E_{\mathrm{e}}(\mathbf{k}) + E_{\mathrm{h}}(\mathbf{k}) \right]^2 + \Delta_{\mathrm{eh}}^2}. \tag{5.10}$$

Because of this mixing, which opens an energy *minigap* at the Fermi energy E_{F}, it was originally expected that intrinsic heterostructures should be semiconducting [38]. However, the anisotropy of the hole band leads to the formation of disconnected Fermi contour islands for most values of E_{F} (*cf.* Fig. 5.7(a) below), reducing the effective minigap and explaining the metallic behaviour seen in most DHET samples [42].

The strength of the electron–hole interaction $\Delta_{\mathrm{eh}}/2$ can be modified either by reducing the overlap between the electron and hole wave functions or by applying a magnetic field in the plane of the heterojunction. An effective means of decreasing the overlap is to introduce an AlSb barrier between the GaSb and the InAs layers. The additional layer increases the spatial separation of the carrier gases; at the same time, the large AlSb band gap ensures that the penetration of the electron and hole states into the barrier is small. If samples with different barrier thicknesses are prepared, Δ_{eh} can be varied systematically [36, 47]. The in-plane magnetic field makes it possible to switch the interaction on and off in a single structure, but does not provide for continuous tuning of Δ_{eh}. The process by which it affects the coupling requires some explanation.

In the presence of a magnetic field, and neglecting spin, the Schrödinger equation (5.4) becomes

$$\frac{[\hat{\mathbf{p}} + e\mathbf{A}(\mathbf{r})]^2}{2m^*}\varphi(\mathbf{r}) + V(z)\varphi(\mathbf{r}) = E_{\text{tot}}\varphi(\mathbf{r}), \tag{5.11}$$

where $\mathbf{A}(\mathbf{r})$ is the magnetic vector potential. If the magnetic field is homogeneous and lies in the plane of the heterostructure along the y-axis, *i.e.*, $\mathbf{B} = (0, B_y, 0)$, the magnetic vector potential can be chosen as $\mathbf{A}(\mathbf{r}) = (B_y z, 0, 0)$ in the Landau gauge.[1] Eqs. (5.1) and (5.11) then lead to the following Schrödinger-like equation in $\chi(z)$ [56]:

$$\frac{\hbar^2}{2m^*}\left(k_x^2 + \frac{2eB_y k_x z}{\hbar} + \frac{e^2 B_y^2 z^2}{\hbar^2} + k_y^2 - \frac{\partial^2}{\partial z^2}\right)\chi(z) + V(z)\chi(z) = E_{\text{tot}}\chi(z). \tag{5.12}$$

Eq. (5.12) is of the form

$$\hat{H}_0\chi(z) + \hat{H}_1\chi(z) = E_{\text{tot}}\chi(z), \tag{5.13}$$

where the Hamiltonian $\hat{H}_0$ in the absence of a magnetic field is given by Eq. (5.6) and

$$\hat{H}_1 = \frac{e^2 B_y^2 z^2}{2m^*} + \frac{\hbar e B_y k_x z}{m^*} \tag{5.14}$$

is the contribution due to B_y [57].

As long as $\hbar e B_y / 2m^* \ll E_0$—which will typically be fulfilled for InAs well thicknesses smaller than 400 Å in the samples discussed here [42, 58]—$\hat{H}_1$ can be treated as a perturbation, leading to a first order energy correction [56, 57]

$$\langle \chi_n | \hat{H}_1 | \chi_n \rangle = \frac{e^2 B_y^2}{2m^*}\langle z^2 \rangle_n + \frac{\hbar e B_y k_x}{m^*}\langle z \rangle_n, \tag{5.15}$$

where $\langle z \rangle_n = \langle \chi_n | z | \chi_n \rangle$ and $\langle z^2 \rangle_n = \langle \chi_n | z^2 | \chi_n \rangle$ denote the expectation values of z and z^2. Rearrangement of $E_{\text{tot}} = E_n + E_{xy} + \langle \chi_n | \hat{H}_1 | \chi_n \rangle$ gives [56, 59]

$$E_{\text{tot}} = E_n + \frac{\hbar^2}{2m^*}\left[\left(k_x + \frac{eB_y}{\hbar}\langle z \rangle_n\right)^2 + k_y^2\right] + \frac{e^2 B_y^2}{2m^*}\left(\langle z^2 \rangle_n - \langle z \rangle_n^2\right). \tag{5.16}$$

From Eq. (5.16) it can be seen that the overall effect of the in-plane field B_y is a shift δk_x of the dispersion relation along the x-direction, which is proportional to the position of

[1] The argument can be extended straightforwardly to $\mathbf{B} = (B_x, B_y, 0)$. $\mathbf{A}(\mathbf{r})$ is then $(B_y z, -B_x z, 0)$.

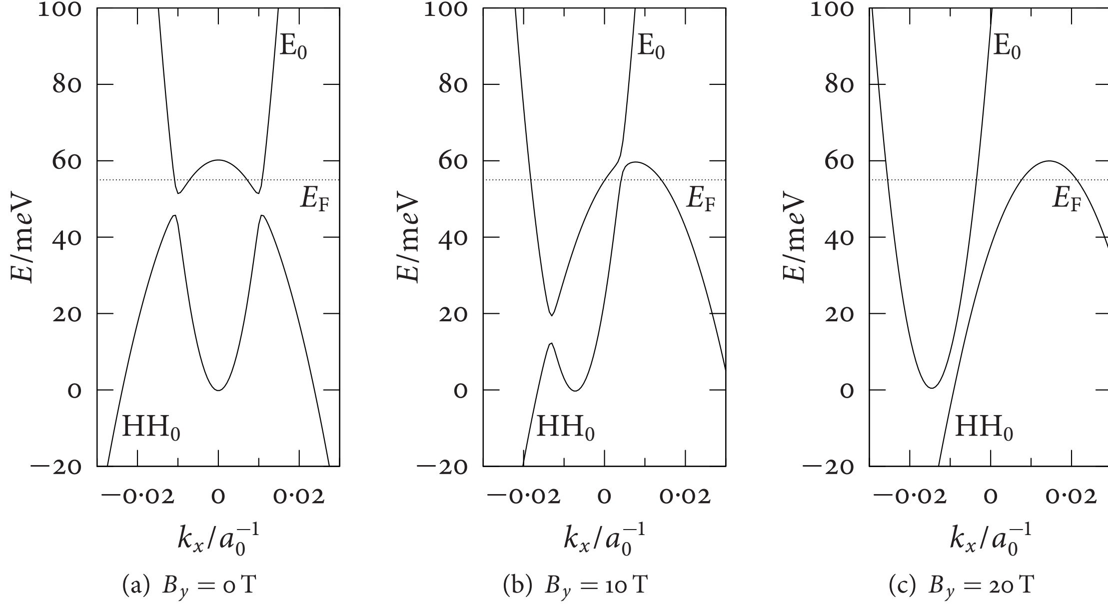

Figure 5.6: Electron and hole dispersion in an in-plane magnetic field, calculated for a DHET with $\Delta = 7\,\mathrm{me}V$, $E_\mathrm{g} = 60\,\mathrm{me}V$, and $\delta z = 180\,\text{Å}$. Wave numbers are given in terms of the Bohr radius a_0.

the electron sheet with respect to the coordinate origin, and a diamagnetic shift δE_n of the subband energy, which depends on the spread of $\chi_n(z)$ [25, 56, 58]:

$$\delta k_x = \frac{eB_y}{\hbar}\langle z\rangle_n; \qquad \delta E_n = \frac{e^2 B_y^2}{2m^*}\left(\langle z^2\rangle_n - \langle z\rangle_n^2\right) \tag{5.17}$$

In the electron-hole system, $\langle z\rangle_n$ can be identified with the distance δz between the electron and hole gases along z, while δE can be neglected [25, 42, 51]; this is in agreement with experiments that have shown little dependence of the subband energies on an in-plane magnetic field [58].

Fig. 5.6 illustrates the effect of the magnetic field on the minigap: Plots of Eq. (5.10) with $E_\pm(k_x, k_y)$ replaced by $E_\pm(k_x \pm \delta k_x/2, k_y)$ are shown for different field strengths and typical values for E_g, E_F, and δz. With increasing field, the crossing points move away from the Fermi level and for sufficiently strong fields, the dispersion curves become decoupled and the minigap disappears.

The effect on the Fermi contours is shown in Fig. 5.7. The relative shift of the disper-

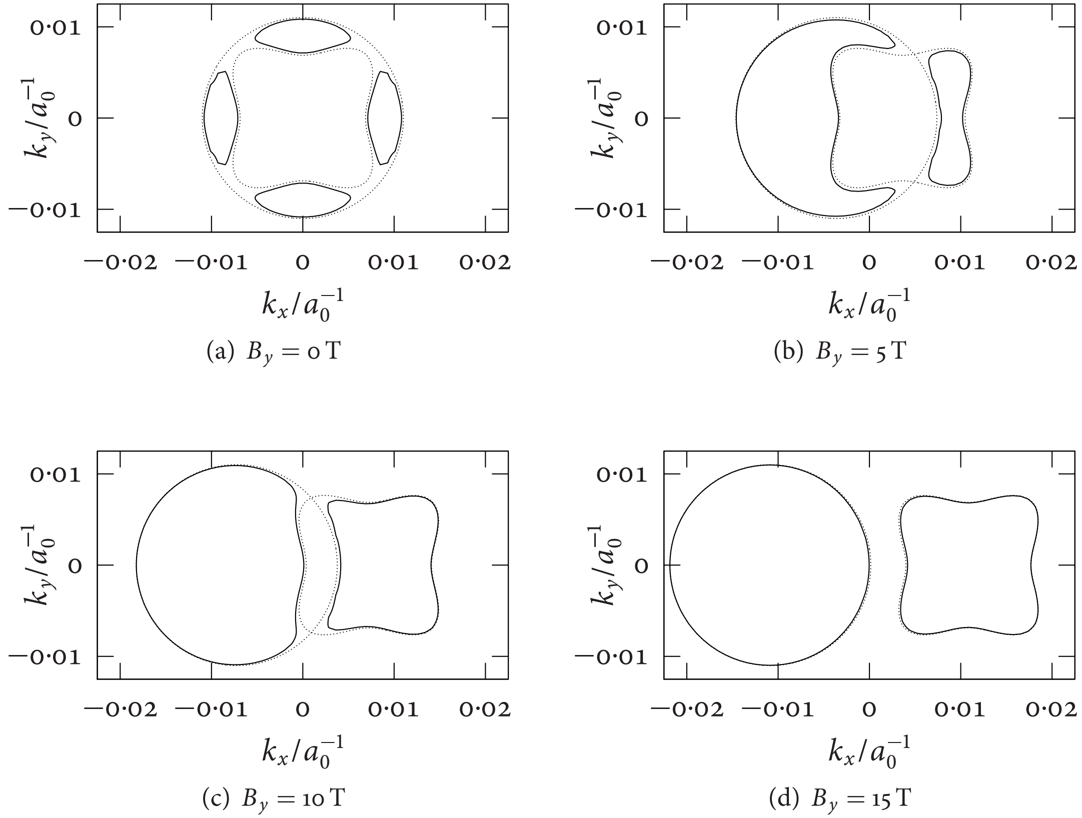

(a) $B_y = 0\,\mathrm{T}$

(b) $B_y = 5\,\mathrm{T}$

(c) $B_y = 10\,\mathrm{T}$

(d) $B_y = 15\,\mathrm{T}$

Figure 5.7: Fermi contours in an in-plane magnetic field, calculated for a DHET with $\Delta = 7\,\mathrm{m}e\mathrm{V}$, $E_\mathrm{g} = 60\,\mathrm{m}e\mathrm{V}$, $\delta z = 180\,\text{Å}$, and $E_\mathrm{F} - E_\mathrm{e}(0) = 55\,\mathrm{m}e\mathrm{V}$. Wave numbers are given in terms of the Bohr radius a_0.

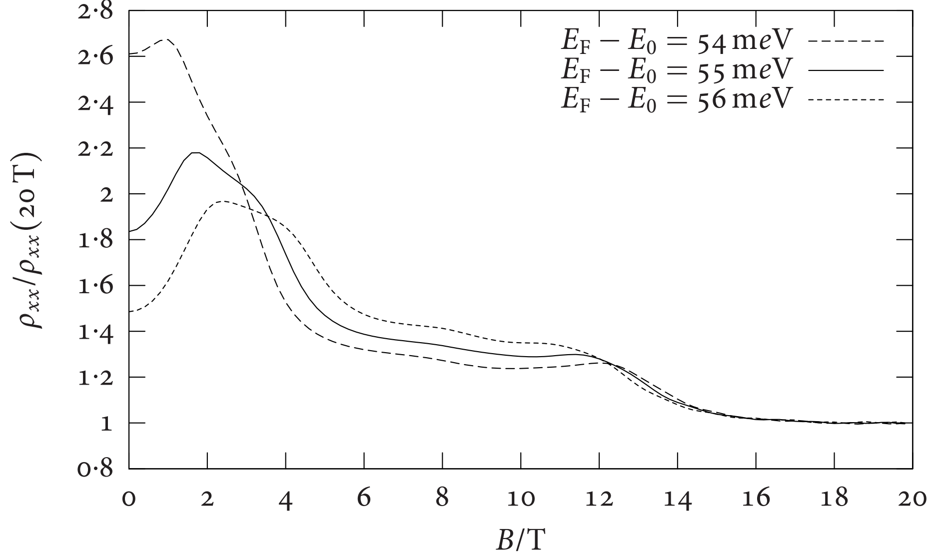

Figure 5.8: Negative magnetoresistance in an in-plane magnetic field, calculated for a DHET with $\Delta = 7\,\mathrm{m}e\mathrm{V}$, $E_\mathrm{g} = 60\,\mathrm{m}e\mathrm{V}$, and $\delta z = 180\,\text{Å}$. The resistivity is given in terms of the resistivity at high field.

sion relations changes the shape of the contours drastically, varying from the small 'puddles' present at zero field to nearly unperturbed independent electron and hole Fermi contours at high field. Owing to the anisotropy of the hole band, the shape in the intermediate region will depend on the orientation of the in-plane field.

The in-plane conductivity, and hence resistivity, can be calculated from the Boltzmann equation (see Appendix B), which leads to an expression of the form

$$\sigma_{xx} = -\frac{2e^2}{(2\pi)^2} \sum_i \int \left[v_x^{(i)}(\mathbf{k})\right]^2 \tau f'\big[E_i(\mathbf{k})\big]\, d\mathbf{k}, \tag{5.18}$$

where $v_x^{(i)}(\mathbf{k})$ is the x-component of the group velocity, $f'(E)$ the derivative of the Fermi-Dirac distribution, and the transport relaxation time τ is taken to be independent of $\mathbf{k}$ [42]. Fig. 5.8 shows the resistivity $\rho_{xx} = 1/\sigma_{xx}$ (since $\rho_{xy} = 0$) calculated by numerical integration from Eq. (5.18) with the simple two-band model of Sec. 5.5.3 and using the same typical values for the sample parameters as in Figs. 5.6 and 5.7. Just as the Fermi contours, the magnetoresistance is highly dependent on the band overlap (not shown) and the Fermi level. Peaks correspond to the field strengths where anticrossing occurs at the Fermi energy, *i.e.*, $\delta k_x(B_y) \approx$

$|k_x^{(e)}(E_F)| - |k_x^{(h)}(E_F)|$ (around 2 T in Fig. 5.8) and $\delta k_x(B_y) \approx |k_x^{(e)}(E_F)| + |k_x^{(h)}(E_F)|$ (around 12 T in Fig. 5.8).

Several studies of GaSb–InAs superlattices and DHETs have shown a large decrease of up to 70 % of the two-dimensional resistivity in the presence of a strong in-plane magnetic field. [42, 50, 54, 58]. The measured magnetoresistance and its temperature dependence are described well by calculations such as those of Fig. 5.8, providing strong evidence for the existence of the minigap. A systematic study of a gated GaSb–InAs heterostructure by Cooper *et al.* [47] has revealed as strong increase in the longitudinal resistance for equal electron and hole concentrations. The temperature dependence of the peak in this experiment indicated an energy gap of *c.* 2 m*e*V, and the resistance increase was not observed in a second sample that was nominally identical save for an AlSb barrier suppressing the electron–hole coupling. Poulter *et al.* [58] have reported optical absorption peaks corresponding to excitation across the minigap, supporting the magnetotransport results. Evidence for a small positive band gap, which disappears in an in-plane electric field, has also been seen in capacitance measurements by Yang *et al.* [60].

5.5.4 Magnetic Breakdown

In a perpendicular magnetic field, carriers follow orbits in the plane of the DHET that in momentum space correspond to orbits along the Fermi contours shown in Fig. 5.7. As a result of the mixing between electron and hole states, the Fermi contour consists of several unconnected islands and the possible closed orbits include both electron- and hole-like states.

The hole states are characterized by a larger effective mass compared to the electron states, so that the carriers take a longer time to complete the hole-like parts of the orbits and are more likely to leave them because of scattering. On the other hand, once the cyclotron energy $\hbar\omega_c$ becomes comparable to the minigap Δ, carriers can tunnel readily between electron-like parts of the Fermi contour, forming an orbit with low effective mass similar to the electron orbit in the absence of electron–hole mixing [61].

The Shubnikov–de Haas-oscillations described in Sec. 5.6.3 and the commensurability features in the presence of a lateral modulation discussed in Chapter 7 are dominated by such *magnetic breakdown orbits* [50], and the evidence for a direct effect of the disjoint Fermi contour islands remains tenuous [51].

5.6 Magnetotransport in a Perpendicular Magnetic Field

5.6.1 Drude Model

It is tempting to describe the parallel magnetotransport in the presence of a perpendicular magnetic field $\mathbf{B} = (0, 0, B_z)$ in terms of a simple semiclassical two-carrier model based on the Drude formalism [25, 50, 51]. In this model, the relaxation time approximation is used and the electrons and holes are assumed to be independent and have individually well-defined conductivities $\boldsymbol{\sigma}_\mathrm{e}$ and $\boldsymbol{\sigma}_\mathrm{h}$. The total conductivity of the electron–hole system would then simply be

$$\boldsymbol{\sigma} = \boldsymbol{\sigma}_\mathrm{e} + \boldsymbol{\sigma}_\mathrm{h}. \tag{5.19}$$

In the Drude model [2], the equation of motion for a particle of species $i \in \{\mathrm{e}, \mathrm{h}\}$ is

$$m_i^* \dot{\mathbf{v}} = q_i \left(\mathbf{E} + \mathbf{v} \times \mathbf{B} \right) - m_i^* \frac{\mathbf{v}}{\tau_i}, \tag{5.20}$$

where $\mathbf{E}$ is the electric field, $\mathbf{v}$ the velocity, m_i^* the effective mass, q_i the charge, and scattering is accounted for by the phenomenological friction term $(m_i^*/\tau_i)\mathbf{v}$ with scattering relaxation time τ_i. If $\mathbf{E} = (E_x, E_y, 0)$, $\mathbf{v} = (v_x, v_y, 0)$, and $\dot{\mathbf{v}} = \mathbf{0}$ Eq. (5.20) simplifies to

$$\frac{v_x}{\mathrm{sgn}(q_i)\mu_i} = E_x + v_y B_z; \qquad \frac{v_y}{\mathrm{sgn}(q_i)\mu_i} = E_y - v_x B_z, \tag{5.21}$$

where $\mu_i \stackrel{\mathrm{def}}{=} |q_i|\tau_i/m_i^*$ is the mobility. Eq. (5.21) has the solution

$$v_x = \frac{\mathrm{sgn}(q_i)\mu_i E_x + \mu_i^2 B_z^2 E_y}{1 + \mu_i^2 B_z^2}; \qquad v_y = \frac{-\mu_i^2 B_z^2 E_x + \mathrm{sgn}(q_i)\mu_i E_y}{1 + \mu_i^2 B_z^2}. \tag{5.22}$$

As the conductivity $\boldsymbol{\sigma}$ is defined by $\mathbf{j} = \boldsymbol{\sigma}\mathbf{E}$ and $\mathbf{j}_i = q_i n_i \mathbf{v}$, where n_i is the carrier concentration, the (x, y)-components of the conductivity tensor $\boldsymbol{\sigma}_i$ are

$$\sigma_{xx}^{(i)} = \sigma_{yy}^{(i)} = \frac{|q_i| n_i \mu_i}{1 + \mu_i^2 B_z^2}; \qquad \sigma_{xy}^{(i)} = -\sigma_{yx}^{(i)} = \frac{q_i n_i \mu_i^2 B_z}{1 + \mu_i^2 B_z^2}. \tag{5.23}$$

For a two-carrier system consisting of electrons and holes Eq. (5.19) together with $\rho_{xx} = \sigma_{xx}/(\sigma_{xx}^2 + \sigma_{xy}^2)$ and $\rho_{xy} = -\sigma_{xy}/(\sigma_{xx}^2 + \sigma_{xy}^2)$ then leads to the following expressions for the in-plane resistivity:

$$\rho_{xx} = \rho_{yy} = \frac{1}{e} \frac{n_\mathrm{e}\mu_\mathrm{e}(1 + \mu_\mathrm{h}^2 B_z^2) + n_\mathrm{h}\mu_\mathrm{h}(1 + \mu_\mathrm{e}^2 B_z^2)}{(n_\mathrm{e}\mu_\mathrm{e} + n_\mathrm{h}\mu_\mathrm{h})^2 + \mu_\mathrm{e}^2\mu_\mathrm{h}^2 B_z^2 (n_\mathrm{e} - n_\mathrm{h})^2}; \tag{5.24}$$

$$\rho_{xy} = -\rho_{yx} = \frac{1}{e} \frac{n_\mathrm{e}\mu_\mathrm{e}^2 B_z(1 + \mu_\mathrm{h}^2 B_z^2) - n_\mathrm{h}\mu_\mathrm{h}^2 B_z(1 + \mu_\mathrm{e}^2 B_z^2)}{(n_\mathrm{e}\mu_\mathrm{e} + n_\mathrm{h}\mu_\mathrm{h})^2 + \mu_\mathrm{e}^2\mu_\mathrm{h}^2 B_z^2 (n_\mathrm{e} - n_\mathrm{h})^2}. \tag{5.25}$$

Eqs. (5.24) and (5.25) exhibit the positive magnetoresistance $\rho_{xx}(B_z)$ and non-linear Hall resistivity $\rho_{xy}(B_z)$ which are characteristic of bipolar systems and have been demonstrated in GaSb–InAs DHETS [50, 51]. Information about n_e, n_h, μ_e, and μ_h could in principle be obtained by fitting the functional dependence on B_z described by these equations to the measured magnetotransport traces.[2]

However, the assumption of independent electrons and holes is ultimately false in the light of the phenomena described in Sec. 5.5.3 and severely limits the applicability of the model to the system investigated here. Depending on the electron–hole ratio and the Fermi level at the DHET, the minigap causes a substantially higher resistivity than scattering alone, and the mobilities are significantly underestimated if such a fit is attempted. Only in the presence of an in-plane magnetic field that is strong enough to completely decouple the electrons and holes the Drude model is a realistic approximation.

[2] Eqs. (5.24) and (5.25) are of the form $y(x) = a(1 + bx^2)/(1 + cx^2)$ and $\eta(x) = \alpha x(1 + \beta x^2)/(1 + \gamma x^2)$, respectively. Each has only three independent parameters, and hence a fit to either $\rho_{xx}(B_z)$ or $\rho_{xy}(B_z)$ cannot be used to determine all four parameters n_e, μ_e, n_h, and μ_h unless one of them is known separately, *e.g.*, n_e from the Shubnikov-de Haas oscillations. If both equations are used, $\gamma = c$, $\alpha = a\sqrt{c}(c - b)/(c - \beta)$, and β remains variable.

5.6.2 Landau Quantization

For a homogeneous magnetic field perpendicular to the (x, y)-plane, *i.e.*, $\mathbf{B} = (0, 0, B_z)$, the magnetic vector potential can be chosen as $\mathbf{A}(\mathbf{r}) = (0, B_z x, 0)$ in the Landau gauge $\nabla_{\mathbf{r}} \cdot \mathbf{A}(\mathbf{r}) = 0$. With the *Ansatz*

$$\varphi(\mathbf{r}) = e^{ik_y y}\chi(z)\psi(x), \tag{5.26}$$

Eq. (5.11) again becomes separable. The equation for $\chi(z)$ is given by Eqs. (5.5) and (5.6), while $\psi(x)$ has to obey

$$\frac{\hbar^2}{2\overline{m}^*}\left(-\frac{\partial^2}{\partial x^2} + k_y^2 + \frac{2eB_z k_y x}{\hbar} + \frac{e^2 B_z^2 x^2}{\hbar^2}\right)\psi(x) + E_n\psi(x) = E_{\text{tot}}\psi(x), \tag{5.27}$$

which simplifies to

$$\left(-\frac{\hbar^2}{2\overline{m}^*}\frac{\partial^2}{\partial \xi^2} + \frac{e^2 B_z^2 \xi^2}{2\overline{m}^*}\right)\psi(\xi) = E_{xy}\psi(\xi) \tag{5.28}$$

with $\xi = x + \hbar k_y/eB_z$ and $E_{xy} = E_{\text{tot}} - E_n$. Eq. (5.28) is the Schrödinger equation of a one-dimensional quantum harmonic oscillator with eigenvalues

$$E_{xy}^{(N)} = \left(N + \frac{1}{2}\right)\hbar\omega_{\text{c}}, \tag{5.29}$$

where the quantum number N is known as the Landau level and $\omega_{\text{c}} = eB_z/\overline{m}^*$ is the cyclotron frequency.

As a result of the quantization, all electron states must be accommodated in the discrete Landau levels. The degeneracy of the Nth Landau level can hence be calculated by considering the number of states that would lie between $E_{xy}^{(N-1)}$ and $E_{xy}^{(N)}$ in the absence of a magnetic field. For the quadratic dispersion relation $E = \hbar(k_x^2 + k_y^2)/2\overline{m}^*$, which follows from Eq. (5.28) if $B_z = 0$, it is straightforward to show [1, 62] that the density of states per unit area of a two-dimensional system is $D(E) = \overline{m}^*/2\pi\hbar^2$ per spin state. In this case, the degeneracy of each Landau level is

$$g_{\text{LL}}(B_z) = \int_{E_{xy}^{(N-1)}}^{E_{xy}^{(N)}} D(E)\,dE = \frac{\overline{m}^*}{2\pi\hbar^2}\hbar\omega_{\text{c}} = \frac{eB_z}{h} = \frac{B_z}{\Phi_0^{(\text{D})}} \tag{5.30}$$

per unit area, where $\Phi_0^{(\mathrm{D})} = h/e$ is the Dirac flux quantum.[3] If n_e is the electron density per unit area, the number of filled spin-split Landau levels at a given field B_z is consequently

$$\nu(B_z) = \frac{n_\mathrm{e}}{g_{\mathrm{LL}}(B_z)} = \frac{n_\mathrm{e}}{B_z/\Phi_0^{(\mathrm{D})}} = \frac{n_\mathrm{e}}{eB_z/h}. \tag{5.31}$$

The quantity $\nu(B_z)$ is known as the (Landau level) filling factor and corresponds to the number of electrons divided by the number of flux quanta.

5.6.3 Shubnikov–de Haas-Oscillations

According to Eq. (5.29), in a magnetic field B_z perpendicular to the plane of the DHET each subband splits into a number of Landau levels that are equally spaced in Energy by $\hbar\omega_\mathrm{c} = \hbar e B_z/\overline{m}^*$. Each Landau level is further split because of the interaction $g^*\mu_\mathrm{B}\mathbf{B}\cdot\boldsymbol{\sigma}$ of the electron spin with the external magnetic field $\mathbf{B}$, which causes an energy shift $\delta E_{xy}^{(N)} = \pm\frac{1}{2}g^*\mu_\mathrm{B}B_z$; here μ_B is the Bohr magneton, g^* is the *effective* gyromagnetic factor of the subband, and $\boldsymbol{\sigma}$ a vector with the Pauli spin matrices as its elements. The corresponding density of states has a peak for each (spin-split) Landau level, which is broadened thermally and by scattering; the contribution due to scattering is $\hbar/\tau$, where τ is the relaxation time. As long as $\omega_\mathrm{c}\tau \gg 1$ and $\hbar\omega_\mathrm{c} \gg k_\mathrm{B}T$, the result is a density of states $D(E)$ that oscillates as a function of energy [1]. If the magnetic field B_z is varied, the period $\hbar\omega_\mathrm{c} = \hbar e B_z/\overline{m}^*$ of this oscillation varies and the Fermi energy E_F successively encounters different Landau levels and a varying density of states. The density of states reaches a minimum if E_F lies between two Landau levels. If spin splitting is not resolved, this occurs at the fields for which the filling factor $\nu(B_z) = \Phi_0^{(\mathrm{D})} n_\mathrm{e}/B_z$ is an even integer, leading to changes in a number of electronic properties that are periodic in $1/B_z$ with a period

$$\Delta_{1/B_z} = \frac{2}{\Phi_0^{(\mathrm{D})} n_\mathrm{e}} = \frac{2e}{n_\mathrm{e} h}. \tag{5.32}$$

[3] Not to be confused with the superconducting flux quantum $\Phi_0^{(\mathrm{s})} = h/2e$.

The periodic change of the magnetic susceptibility is called the de Haas–van Alphen-effect, while the corresponding magnetoresistance fluctuations are known as Shubnikov–de Haas-oscillations.

The oscillations are a useful tool for the characterization of GaSb–InAs DHETs. In these structures, a single $1/B_z$ oscillation frequency is typically observed in the magnetoresistance [50, 51], which can be attributed to electron-like magnetic breakdown orbits as explained in Sec. 5.5.4 and hence corresponds to the InAs conduction band. In this situation, Eq. (5.32) provides an accurate estimate of the two-dimensional electron density.

5.7 Sample Growth using Metal-Organic Vapour Phase Epitaxy

5.7.1 Motivation

Semiconductor heterostructures can be grown epitaxially[4] on the surface of suitable substrate wafers by several different techniques. The most widely used technology is molecular beam epitaxy (MBE), which uses ballistic beams of atoms or molecules created by controlled evaporation of precursor materials in ultra-high vacuum (UHV). The samples discussed in this thesis were grown in Oxford by a variety of vapour phase epitaxy (VPE) that is known as metal-organic vapour phase epitaxy (MOVPE) as it uses metal-organic precursor materials. A third option is liquid phase epitaxy (LPE).

MBE produces high quality materials and allows excellent reproducibility and control of the epitaxial growth down to monolayer accuracy.[5] Its drawback is the reliance on UHV, which not only imposes high demands on the quality of the vacuum equipment but also reduces its flexibility: If the vacuum in the growth chamber is compromised for any reason, reestablishing it usually takes several weeks. MOVPE can grow semiconductors with similar and in some cases better quality while operating at pressures that do not present a technological challenge. However, monolayer accuracy cannot be achieved and reproducibility can

[4] From Greek ἐπί, 'upon', and τάττειν, 'to arrange'. In Greek, ἐπίταξις actually means 'command'.
[5] Abrupt interfaces, however, may not be thermodynamically stable.

be an issue as the growth depends on a large number of parameters. Also, the metal-organic precursors are highly toxic[6] and costly hazard management is necessary.

5.7.2 Principles of Metal-Organic Vapour Phase Epitaxy

MOVPE was first described in 1969 by Manasevit and Simpson [63]. In this technique, the substrate wafer is placed in a reaction chamber on a heated sample holder. A continuous flow of hydrogen carrier gas, in which a controlled amount of the precursor materials has been dissolved, is maintained at the substrate. The metal-organic precursors are cracked by pyrolysis[7] at the elevated temperatures occurring close to the sample surface. Metal atoms then diffuse across the low-velocity boundary layer to the substrate, where they are adsorbed at the surface and lose any remaining organic groups. These groups react to form volatile organic compounds, while the metals diffuse along the surface until they are incorporated in the crystal lattice.

The controlled solutions of the precursors in hydrogen are obtained by driving dry hydrogen gas through bubblers each containing a liquid precursor. The bubblers are kept at a well-defined temperature and the H_2 gas passing through them takes up precursor molecules and forms a saturated solution, which is then mixed with pure hydrogen at the desired dilution. The dilution ratio and the flows of the process gases are regulated with the help of mass flow controllers. Individual precursor solutions can be quickly switched into and out of the mixing manifold that feeds the process chamber.

For epitaxial growth to be possible, the substrate must be free from contaminants and oxide. This can be achieved by creating an oxide layer with desirable properties by etching and controlled oxidation.[8] The oxide layer is then removed by thermal desorption in the MOVPE reactor in the presence of either pure hydrogen or the process gas providing the substrate species with the highest vapour pressure to prevent the preferential loss this element.

[6] In the proper sense of being quite lethal should they escape during normal operation.
[7] from Greek πῦρ, 'fire' and λύειν 'to dissolve'
[8] Nowadays, so-called 'epi-ready' wafers with suitable surfaces are available commercially, so that this process need not be performed in the laboratory.

The main controlling parameters of MOVPE growth are the relative flow rates of the process gases and the substrate temperature, while the fluid dynamics of the mixing of the individual gases and the flow in the process chamber also play an important part. Different reactor geometries in which the sample holder is oriented either parallel or perpendicular to the gas flow can be used.

5.7.3 Growth of Epitaxial GaSb–InAs Heterostructures in Oxford

The samples discussed in this thesis were grown in the Clarendon Laboratory in Oxford by Nigel Mason and Philip Shields. The reactor, which has now been decommissioned, operated near atmospheric pressure and used a reaction chamber made from glass in which the sample surface was oriented horizontally and aligned parallel to the main gas flow [37]. The substrate wafers rested on a molybdenum susceptor which was heated from underneath by a resistive heater cut from a sheet of manganese metal. Despite the fact that the temperature was monitored with a thermocouple, there is a large uncertainty of at least 30 °C in the measurement of the absolute growth temperature; the reproducibility and relative accuracy, however, was much better unless the replacement of the heater became necessary.

GaSb–InAs heterostructures were grown on lattice-mismatched (by approximately 7·3 %) semi-insulating undoped GaAs wafers. Such wafers are readily procurable commercially, while good quality GaSb wafers are still expensive. More importantly, GaSb wafers are inevitably p-type, which is undesirable for electrical measurements on epitaxially grown devices [16, 64, 65]. Following a thin GaAs layer and a low temperature heteroepitaxial GaSb layer, a relaxed GaSb buffer layer of roughly 2 μm thickness was grown on the GaAs substrate, creating a *virtual substrate* for the growth of the heterostructures. Under optimal conditions, much of the strain caused by the large lattice mismatch at the GaAs–GaSb interface is accommodated by 90° misfit dislocations in the plane of the interface [65]. Together with the mutual annihilation of threading dislocations during the growth of the buffer layer [66], this results in a virtual substrate relatively free of dislocations. The surface morphology of

such GaSb layers was generally characterized by flat elongated pyramidal shapes 10 to 30 nm high and several micrometres wide. The DHETs grown on these virtual substrates closely follow the shape of the surface; on the scale of these features, the surface roughness was *not* correlated with electrical indicators of the epilayer quality. While the pyramids may affect transport in the DHETs by causing a local tilt with respect to the plane of the sample and by changing the states at the resulting kink lines, the overall effect is assumed to be small.

Trimethylgallium (TMGa), trimethylantimony (TMSb), trimethylindium (TMIn), and tertiarybutylarsine (TBAs) were used as precursors. For growth of GaSb, the ratio of gallium to antimony at the surface needs to be close to 1 as Sb has a very low vapour pressure compared to Ga and would otherwise be precipitated at the growth front. A further complication is caused by the incomplete pyrolysis of the precursors at typical GaSb growth temperatures, leading to a growth rate that is dependent on temperature, *i.e.*, kinetically controlled [16, 22]. Fortunately the pyrolysis rate temperature dependence of TMGa and TMSb are very similar, so that the precursor ratio required at the gas inlet depends only weakly on temperature [16]. The 'epi-ready' GaAs wafers were deoxidized at 650 to 700 °C in the presence of TBAs; GaSb and InAs were typically grown at 525 to 600 °C and 500 to 525 °C, respectively. However, the values were affected by a relatively large absolute uncertainty as explained above, and the optimal growth conditions had to be determined anew after any significant modification to the reactor.

The crystal growth could be monitored *in situ* with the help of a surface photoabsorption (SPA) setup. In this method, a laser is incident on the semiconductor surface at an angle close to Brewster's angle, and the intensity of the reflected light with its (electric field) polarization parallel to the surface is recorded. In our reactor, a 633 nm laser was used at Brewster's angle for GaAs (75·3° [67]) and the reflected signal was detected by a silicon photodiode using a lock-in technique [68, 69]. Information on the surface roughness, surface composition, and heterostructure layer thickness could be obtained. SPA is sensitive to the surface material via the difference in Brewster's angle, and to epilayer thickness via interference between light

reflected from the surface and the heterointerface, which results in Fabry-Pérot oscillations. The measurement of the layer thickness in particular was an important tool in the calibration of the growth rates.

5.8 Overview of Individual Samples

A number of MOVPE-grown single- and double-layer GaSb–InAs heterostructures with different layer thicknesses were investigated for this thesis. As explained in Sec. 5.7, MOVPE is strongly dependent on growth conditions, while absolute reproducibility is not assured. As a result, there is considerable variation in the properties of nominally identical structures [22].

The DHETs are listed in Table 5.1 with their properties. Electron concentrations and, where available, hole concentrations have been quoted. The electron mobility μ_e can be estimated from the sheet resistivity $\rho_{xx}(0)$ in the absence of a perpendicular magnetic field as $\mu_\mathrm{e} \approx 1/[en_\mathrm{e}\rho_{xx}(0)]$ by setting B_z in Eq. (5.24) to zero and assuming $n_\mathrm{e}\mu_\mathrm{e} \gg n_\mathrm{h}\mu_\mathrm{h}$. (Multiple parameter fits of Eqs. (5.24) and (5.25) to the observed longitudinal and Hall resistivities as a function of perpendicular field indicate that $\mu_\mathrm{e}/\mu_\mathrm{h}$ is typically of the order 10.) As explained in Secs. 5.5.3 and 5.6.1, a more realistic estimated will be obtained from the minimal value of ρ_{xx} in a high parallel magnetic field.

As may be expected, the electronic properties will in general vary slightly between different parts of the same epitaxial structures, and this variation can become quite noticeable for large samples or ones that were grown under less than optimal conditions. No attempt was made to average over different parts of such samples; the values quoted here correspond to a single location deemed representative.

The observed properties of these samples fit the expectation put forward in Sec. 5.5.2 that the electron–hole-ratio is strongly affected by the presence of nearby surface states: The samples of the OX37*xx* varying cap thickness series show a decreasing hole sheet density as the cap thickness decreases from approximately 1,200 Å to 800 Å. Even thinner cap samples

Sample	t_{well} (Å)	t_{cap} (Å)	n_{SdH} ($10^{11}/cm^2$)	n_h ($10^{11}/cm^2$)	$\rho_{xx}(0)$ (Ω/□)	$\rho_{xx}(B_\parallel)$ (Ω/□)
OX3735	250	600	9·4		220	
OX3729	250	800	7·8†	3·7†	40†	
OX3730	250	1,000	8·0†	5·2†	40†	
OX3733	250	1,200	7·9†	6·1†	56†	
OX4256	(300)	(1,000)	8·0		40	
OX4338	(300)	—	16·0		256	
OX4340	(300)	(1,200)	7·0		186	
OX4434	(300)	(700)	7·9		74	
OX4529	300	1,000	7·7		66	
OX4530	300	700	7·9		112	
OX4531	300	500	11·5		75	
OX4532	300	680	7·1		110*	47*
OX4532′	300	380	12·0		81*	59*
OX4576	300	1,500	6·7		141	124
OX4576′	300	600	7·8		187	

Table 5.1: DHET samples grown by MOVPE. Most InAs well and GaSb cap thicknesses t_{well}, and t_{cap} were estimated from SPA traces and are accurate to about 5 %; values in brackets were deduced from the growth rate and are accurate to about 20 %. The carrier concentration n_{SdH} was calculated from the frequency of the Shubnikov–de Haas-oscillations in the perpendicular field magnetoresistance and corresponds to the electron concentration n_e; it is accurate to about 2×10^{10} cm^{-2} for a specific piece of the sample. Both the zero field value and the minimal value in a parallel magnetic field are given for the sheet resistivity. Most measurements were taken at 4·2 K. Values marked with an asterisk (∗) were measured at 1·5 K. The data marked with a dagger (†) were measured by Takashina [51] at 50 mK; the hole concentration was estimated from the compensated quantum Hall effect.

Sample	t_1 (Å)	t_{sp} (Å)	t_2 (Å)	t_{cap} (Å)	n_{SdH} (10^{11}/ cm^2)	$\rho_{xx}(0)$ ($\Omega/\square$)	$\rho_{xx}(B_\parallel)$ ($\Omega/\square$)
OX4536	200	50	200	1,500	6·2	118	35
OX4559	200	100	200	1,500	6·2	212	130
OX4538	250	25	250	3,400	6·4	232	178
OX4533	250	50	250	1,500	6·7	71	62
OX4544	250	100	250	2,600	7·6	10	(10)
OX4564	300	50	300	1,500	7·2	124	82
OX4563	300	100	300	1,500	7·3	128	30
OX4574	300	200	300	1,500	6·9	82	21
OX4575	300	300	300	1,500	6·5	82	32
OX4576	—	—	300	1,500	6·7	141	124

Table 5.2: Double well samples grown by MOVPE. The InAs well, GaSb spacer, and GaSb cap thicknesses t_1, t_2, t_{sp}, and t_{cap} were estimated from SPA traces and are accurate to about 5 %. The carrier concentration was calculated from the frequency of the Shubnikov–de Haas-oscillations in the perpendicular field magnetoresistance and is accurate to 2×10^{10} cm^{-2} for a specific piece of the sample. Both the zero field value and the minimal value in a parallel magnetic field are given for the sheet resistivity. Measurements were taken at 4·2 K.

(OX3735, OX4531, OX4532′) also have an increased electron sheet density. The behaviour of OX4532′ and OX4576′, which were created from OX4532 and 4576, respectively, by removing part of the GaSb cap by reactive ion etching (RIE), supports this picture: In both cases the electron sheet density was increased significantly.

Table 5.2 shows the double InAs well samples ordered by well and spacer thickness. These samples are discussed in detail in Chapter 6. Where available, the minimum of the longitudinal sheet resistivity $\rho_{xx}(B_\parallel)$ as a function of the in-plane magnetic field is invariably[9] significantly lower than the magnitude of the resistivity in the absence of a parallel field, substantiating the claims about the presence of a minigap made in Sec. 5.5.3 on the basis of previous work.

[9] With the exception of the double well sample OX4544, which has an unusually low $\rho_{xx}(0)$.

5.9 Summary

The *broken gap* band arrangement of GaSb–InAs heterostructures, in which the InAs conduction band lies lower in energy than the GaSb valence band, leads to charge transfer from the GaSb to the InAs layers, forming intrinsic populations of mobile electrons and holes without the need for doping. For thin InAs wells, quantization of the confinement energy becomes relevant at low temperatures, leading to quasi-two-dimensional behaviour as the carrier wave functions are restricted in the growth direction to a number of states corresponding to discrete subband energies.

Because the electrons and holes in adjacent layers interact, hybrid states appear and a minigap opens in the dispersion relation close to the Fermi level. The effect of this minigap can be seen in the strong negative parallel field magnetoresistance observed in single- and multilayer structures and in radiative transitions. It is not directly observed in experiments probing cyclotron motion because of magnetic breakdown, *i.e.*, tunnelling across the minigap once the cyclotron energy becomes comparable to the interaction energy.

A large number of GaSb–InAs heterostructures were grown in Oxford by MOVPE. The technique allows the creation of high-quality intrinsic samples, but is somewhat unpredictable, necessitating careful characterization of individual specimens. Both Landau quantization in a perpendicular magnetic field—via the analysis of Shubnikov–de Haas-oscillations—and a semiclassical transport theory can be used for this purpose. The accurate determination of hole concentrations and mobilities, however, remains elusive as the presence of the minigap severely limits the applicability of the semiclassical model.

A number of specific growth samples have been introduced in relation to the theoretical treatment; these samples will form the basis for the discussion in the following chapters.

Bibliography

[1] C. Weisbuch and B. Vintner. *Quantum Semiconductor Structures*. Academic Press, San Diego, California, 1991.

[2] N. W. Ashcroft and D. N. Mermin. *Solid State Physics*. Harcourt College Publishers, Fort Worth, Texas, college edition, 1976.

[3] H. Kroemer. The 6·1 Å family (InAs, GaSb, AlSb) and its heterostructures: a selective review. *Physica E*, 20:196–202, 2003.

[4] S. M. Sze. *Physics of Semiconductor Devices*. John Wiley & Sons, New York, second edition, 1981.

[5] C. Kittel. *Introduction to Solid State Physics*. John Wiley & Sons, New York, seventh edition, 1996.

[6] M. L. Cohen and T. K. Bergstresser. Band structures and pseudopotential form factors for fourteen semiconductors of the diamond and zinc-blende structures. *Physical Review*, 141(2):789–796, January 1966.

[7] I. Topol, H. Neumann, and E. Hess. Band structure of AlSb. *Czechoslovak Journal of Physics B*, 24:107–112, 1974.

[8] J. R. Chelikowsky and M. L. Cohen. Nonlocal pseudopotential calculations for the electronic structure of eleven diamond and zinc-blende semiconductors. *Physical Review B*, 14(2):556–582, July 1976.

[9] Z. M. Fang, K. Y. Ma, D. H. Jaw, R. M. Cohen, and G. B. Stringfellow. Photoluminescence of InSb, InAs, and InAsSb grown by organometallic vapor phase epitaxy. *Journal of Applied Physics*, 67(11):7034–7039, June 1990.

[10] M.-C Wu and C.-C. Chen. Photoluminescence of high-quality GaSb grown from Ga- and Sb-rich solutions by liquid-phase epitaxy. *Journal of Applied Physics*, 72(9):4275–4280, November 1992.

[11] I. Vurgaftman, J. R. Meyer, and L. R. Ram-Mohan. Band parameters for III–V compound semiconductors and their alloys. *Journal of Applied Physics*, 89(11):5815–5875, June 2001.

[12] L. L. Chang and L. Esaki. Electronic properties of InAs–GaSb superlattices. *Surface Science*, 98:70–89, 1980.

[13] G. Tuttle, H. Kroemer, and J. H. English. Electron concentrations and mobilities in AlSb/InAs/AlSb quantum wells. *Journal of Applied Physics*, 65(12):5239–5342, June 1989.

[14] G. Tuttle, H. Kroemer, and J. H. English. Effects of interface layer sequencing on the transport properties of InAs/AlSb quantum wells: Evidence for antisite donors in the InAs/AlSb interface. *Journal of Applied Physics*, 67(6):3032–3037, March 1990.

[15] C. Nguyen, B. Brar, H. Kroemer, and J. H. English. Surface donor contribution to electron sheet concentrations in not-intentionally doped InAs–AlSb quantum wells. *Applied Physics Letters*, 60(15):1854–1856, April 1992.

[16] A. Aardvark, N. J. Mason, and P. J. Walker. The growth of antimonides by MOVPE. *Progress in Crystal Growth and Characterization*, 35(2–4):207–241, 1997.

[17] Y. Chen, D. M. Symons, M. Lakrimi, A. Salesse, G. B. Houston, R. J. Nicholas, N. J. Mason, and P. J. Walker. One dimensional transport and gating of InAs/GaSb structures. *Superlattices and Microstructures*, 15(1):41–45, 1994.

[18] M. S. Daly, K. S. H. Dalton, M. Lakrimi, N. J. Mason, R. J. Nicholas, M. van der Burgt, P. J. Walker, D. K. Maude, and J. C. Portal. Zero-Hall-resistance state in a semimetallic InAs/GaSb superlattice. *Physical Review B*, 53(16):10524–10527, April 1996.

[19] R. J. Nicholas, M. Lakrimi, B. Kardynał, S. Khym, N. J. Mason, J. Rehman, K. Takashina, P. J. Walker, D. M. Symons, D. K. Maude, and J. C. Portal. A digital quantum Hall effect. *Physica E*, 6:836–839, 2000.

[20] A. C. Jones. Metalorganic precursors for vapour phase epitaxy. *Journal of Crystal Growth*, 129:728–773, 1993.

[21] M. Behet, R. Hövel, A. Kohl, A. Mesquida Küsters, B. Opitz, and K. Heime. MOVPE growth of III-V compounds for optoelectronic and electronic applications. *Microelectronics Journal*, 27:297–334, 1996.

[22] R. M. Biefeld. The metal-organic chemical vapor deposition and properties of III–V antimony-based semiconductor materials. *Materials Science and Engineering R*, 36:105–142, 2002.

[23] M. Larkimi, R. W. Martin, N. J. Mason, R. J. Nicholas, and P. J. Walker. GaSb/InAs heterojunctions grown by MOVPE: effect of gas switching sequences on interface quality. *Journal of Crystal Growth*, 110:677–682, 1991.

[24] R. G. Dandrea, C. B. Duke, and A. Zunger. Interfacial atomic structure and band offsets at semiconductor heterojunctions. *Journal of Vacuum Science and Technology B*, 10(4):1744–1753, July/August 1991.

[25] C. Petchsingh. *Cyclotron Resonance Studies on InAs/GaSb Heterostructures*. DPhil thesis, Wolfson College, University of Oxford, 2002.

[26] J. Spitzer, A. Höpner, M. Kuball, M. Cardona, B. Jenichen, H. Neuroth, B. Brar, and H. Kroemer. Influence of the interface composition of InAs/AlSb superlattices on their optical and structural properties. *Journal of Applied Physics*, 77(2):811–820, January 1995.

[27] C. R. Bolognesi, H. Kroemer, and J. H. English. Interface roughness scattering in InAs/AlSb quantum wells. *Applied Physics Letters*, 61(2):213–215, July 1992.

[28] I. Sela, C. R. Bolognesi, L. A. Samoska, and H. Kroemer. Study of interface composition and quality in AlSb/InAs/AlSb quantum wells by Raman scattering from interface modes. *Applied Physics Letters*, 60(26):3283–3285, June 1992.

[29] B. R. Bennet, R. Magno, and N. Papanicolaou. Controlled n-type doping of antimonides and arsenides using GaTe. *Journal of Crystal Growth*, 251:532–537, 2003.

[30] C. R. Bolognesi, M. W. Dvorak, and D. H. Chow. High-transconductance delta-doped InAs/AlSb HFET's with ultrathin silicon-doped InAs quantum well donor layer. *IEEE Electron Device Letters*, 19(3):83–85, March 1998.

[31] C. R. Bolognesi, M. W. Dvorak, and D. H. Chow. InAs/AlSb heterostructure field-effect transistors using a Si-doped InAs/AlSb short-period superlattice modulation doping barrier. *Journal of Vacuum Science and Technology A*, 16(2):843–845, March/April 1998.

[32] C. R. Bolognesi, M. W. Dvorak, and D. H. Chow. Impact ionization suppression by quantum confinement: Effects on the DC and microwave performance of narrow-gap channel InAs/AlSb HFET's. *IEEE Transactions on Electron Devices*, 46(5):826–832, May 1999.

[33] S. J. Koester, C. R. Bolognesi, M. Thomas, E. L. Hu, and H. Kroemer. Determination of one-dimensional subband spacings in InAs/AlSb ballistic constrictions using magentic-field measurements. *Physical Review B*, 50(8):5710–5712, August 1994.

[34] S. J. Koester, B. Brar, C. R. Bolognesi, E. J. Caine, A. Patlach, E. L. Hu, H. Kroemer, and M. J. Rooks. Length dependence of quantized conductance in ballistic constrictions fabricated on InAs/AlSb quantum wells. *Physical Review B*, 53(19):13063–13073, May 1996.

[35] M. Drndic, M. P. Grimshaw, L. J. Cooper, and D. A. Ritchie. Tunable electron-hole gases in gated InAs/GaSb/AlSb systems. *Applied Physics Letters*, 70(4):481–483, January 1997.

[36] T. P. Marlow, L. J. Cooper, D. D. Arnone, N. K. Patel, D. M. Whittaker, E. H. Linfield, D. A. Ritchie, and M. Pepper. Ground state of a two-dimensional coupled electron-hole gas in inas/gasb narrow gap heterostructures. *Physical Review Letters*, 82(11):2362–2365, March 1999.

[37] G. R. Booker, M. Daly, P. C. Klipstein, M. Lakrimi, T. F. Kuech, J. Li S. G. Lyapin, N. J. Mason, I. J. Murgatroyd, J.-C. Portal, R. J. Nicholas, D. M. Symons, P. Vicente, and P. J. Walker. Growth of InAs/GaSb strained layer superlattices by MOVPE: III. Use of UV absorption to monitor alkyl stability in the reactor. *Journal of Crystal Growth*, 170:777–782, 1997.

[38] M. Altarelli. Electronic structure and semiconductor-semimetal transition in InAs–GaSb superlattices. *Physical Review B*, 28(2):842–845, July 1983.

[39] S. Datta, M. R. Melloch, and R. L. Gunshor. Possibility of an excitonic ground state in quantum wells. *Physical Review B*, 32(4):2607–2609, August 1985.

[40] J.-P. Cheng, J. Kono, B. D. McCombe, I. Lo, W. C. Mitchel, and C. E. Stutz. Evidence for a stable excitonic ground state in a spatially separated electron–hole system. *Physical Review Letters*, 74(3):450–453, January 1995.

[41] T. A. Vaughan. *Magneto-optics of InAs/GaSb Heterostructures*. DPhil thesis, Brasenose College, University of Oxford, 1995.

[42] M. Lakrimi, S. Khym, R. J. Nicholas, D. M. Symons, F. M. Peeters, N. J. Mason, and P. J. Walker. Minigaps and novel giant negative magnetoresistance in InAs/GaSb semimetallic superlattices. *Physical Review Letters*, 79(16):3034–3037, October 1997.

[43] M. S. Daly, D. M. Symons, M. Lakrimi, R. J. Nicholas, N. J. Mason, and P. J. Walker. Interface composition dependence of the band offset in InAs/GaSb. *Semiconductor Science and Technology*, 11:823–826, 1996.

[44] M. S. Daly, D. M. Symons, M. Lakrimi, R. J. Nicholas, N. J. Mason, and P. J. Walker. Interface composition dependence of the band offset in InAs/GaSb. *Surface Science*, 361/362:205–208, 1996.

[45] Y. Naveh and B. Laikhtman. Band-structure tailoring by electric field in a weakly coupled electron-hole system. *Applied Physics Letters*, 66(15):1980–1982, April 1995.

[46] G. L. B. Houston, Y. Chen, J. Singleton, N. J. Mason, and P. J. Walker. The interface properties of MIS structures on anodically oxidized GaSb. *Semiconductor Science and Technology*, 12:1140–1146, 1997.

[47] L. J. Cooper, N. K. Patel, V. Drouot, E. H. Linfield, D. A. Ritchie, and M. Pepper. Resistance resonance induced by electron-hole hybridization in a strongly coupled inas/gasb/alsb heterostructure. *Physical Review B*, 57(19):11915–11918, May 1998.

[48] M. J. Yang, F.-C. Wang, C. H. Yang, B. R. Bennett, and T. Q. Do. A composite quantum well field-effect transistor. *Applied Physics Letters*, 69(1):85–87, July 1996.

[49] F. Rahman, B. L. Gallagher, M. Behet, and J. De Boeck. Gating of inas/gasb quantum wells using a silicon monoxide gate insulator. *Applied Physics Letters*, 73(1):88–90, July 1998.

[50] Y. J. Rehman. *Processing and Magneto-transport Studies of InAs/GaSb Low Dimensional Structures*. DPhil thesis, The Queen's College, University of Oxford, 1999.

[51] K. Takashina. *Magneto-transport Studies of GaSb/InAs/GaSb Double-heterostructures*. DPhil thesis, University College, University of Oxford, 2002.

[52] M. Altarelli, J. C. Maan, L. L. Chang, and L. Esaki. Electronic states and quantum Hall effect in GaSb–InAs–GaSb quantum wells. *Physical Review B*, 35(18):9867–9870, June 1987.

[53] M. S. Daly, D. M. Symons, M. Lakrimi, R. J. Nicholas, N. J. Mason, and P. J. Walker. Interface composition dependence of the band offset in InAs/GaSb. *Semiconductor Science and Technology*, 11:823–826, 1996.

[54] M. Lakrimi, S. Khym, D. M. Symons, R. J. Nicholas, F. M. Peeters, N. J. Mason, and P. J. Walker. Mini-gaps and novel giant negative magnetoresistance in InAs/GaSb semimetallic superlattices. *Physica E*, 2:363–367, 1998.

[55] *Landolt-Börnstein Numerical Data and Functional Relationships in Science and Technology: New Series: Group III: Crystal and Solid State Physics*, volume 17. Springer, 1982.

[56] K. K. Choi, B. F. Levine, N. Jarosik, J. Walker, and R. Malik. Anisotropic magnetotransport in weakly coupled GaAs–$Al_xGa_{1-x}As$ multiple quantum wells. *Physical Review B*, 38(17):12362–12368, 1988.

[57] F. Stern. Transverse Hall effect in the electric quantum limit. *Physical Review Letters*, 21(25):1687–1690, December 1968.

[58] A. J. L. Poulter, M. Lakrimi, R. J. Nicholas, N. J. Mason, and P. J. Walker. Optical probing of the minigap in InAs/GaSb semimetallic superlattices. *Physica B*, 256–258:256–259, 1998.

[59] W. Beinvogl, A. Kamgar, and J. F. Koch. Influence of a magnetic field on electron subbands in a surface-charge layer. *Physical Review B*, 14(10):4274–4289, November 1976.

[60] M. J. Yang, C. H. Yang, B. R. Bennett, and B. V. Shanabrook. Evidence of a hybridization gap in "semimetallic" InAs/GaSb systems. *Physical Review Letters*, 78(24):4613–4616, June 1997.

[61] D. M. Symons, M. Lakrimi, R. J. Nicholas, D. K. Maude, J. C. Portal, N. J. Mason, and P. J. Walker. Magnetic breakdown in the semimetallic InAs/GaSb system. *Physical Review B*, 58(11):7292–7299, September 1998.

[62] T. Ando, A. B. Fowler, and F. Stern. Electronic properties of two-dimensional systems. *Reviews of Modern Physics*, 54(2):437–672, April 1982.

[63] H. M. Manasevit and W. I. Simpson. Use of metal-organics in preparation of semiconductor materials. I. Epitaxial gallium-V compounds. *Journal of The Electrochemical Society*, 116:1725–1732, 1969.

[64] S. V. Ivanov, P. D. Altukhov, T. S. Argunova, A. A. Bakun, A. A. Budza, V. V. Chaldyshev, Yu. A. Kovalenko, P. S. Kop'ev, R. N. Kutt, B. Ya. Meltser, S. S. Ruvimov, S. V. Shaposhnikov, L. M. Sorokin., and V. M. Ustinov. Molecular beam epitaxy growth and characterization of thin ($< 2\,\mu m$) GaSb layers on GaAs(100) substrates. *Semiconductor Science and Technology*, 8:347–356, 1993.

[65] W. Qian, M. Skowronski, R. Kaspi, M. De Graef, and V. P. David. Nucleation of misfit and threading dislocations during epitaxial growth of GaSb on GaAs(001) substrates. *Journal of Applied Physics*, 81(11):7268–7272, June 1997.

[66] P. M. Thibado, B. R. Bennett, M. E. Twigg, B. V. Shanabrook, and L. J. Whitman. Evolution of GaSb epitaxy on GaAs(001)-c(4×4). *Journal of Vacuum Science and Technology A*, 14(3):885–890, May/June 1996.

[67] C. W. Bumby. *Thermophotovoltaic Devices based upon Heteroepitaxial GaSb grown by MOVPE*. DPhil thesis, Hertford College, University of Oxford, 2005.

[68] D. A. Allwood, N. J. Mason, and P. J. Walker. In situ characterisation of MOVPE by surface photoabsorption: I. Substrate oxide desorption. *Journal of Crystal Growth*, 195:163–167, 1998.

[69] P. C. Klipstein, S. G. Lyapin, N. J. Mason, and P. J. Walker. In situ characterisation of MOVPE by surface photoabsorption: II. Interface monitoring. *Journal of Crystal Growth*, 195:168–173, 1998.